Highlights

Quadrature by Two Expansions: Evaluating Laplace Layer Potentials using Complex Polynomial and Plane Wave Expansions

Lingyun Ding, Jingfang Huang, Jeremy L. Marzuola, Zhuochao Tang

- We compare the errors from the classical QBX and new QB2X methods inside one leaf box where the boundary curve is described by $s(\tilde{x}) = \tilde{x}^2 + \frac{\tilde{x}^3}{10} - 2\tilde{x}^4$. For the QBX method, even though the errors decay rapidly in the regions close to the expansion center, because of the extreme nonlinear dependency on the geometry, the $||err||_\infty$ in the entire leaf box are 6.0×10^{-2} and 1.9×10^{-2} when $K = 40$ and $K = 100$, respectively (also see Fig. 12). This very slow convergence means that several expansions with different expansion centers have to be used for this particular leaf box. In existing QBX+FMM implementations, accuracy is achieved by either requesting more refinement levels in the FMM hierarchical adaptive tree structures, or using several expansions with different centers in the same leaf box, or both.

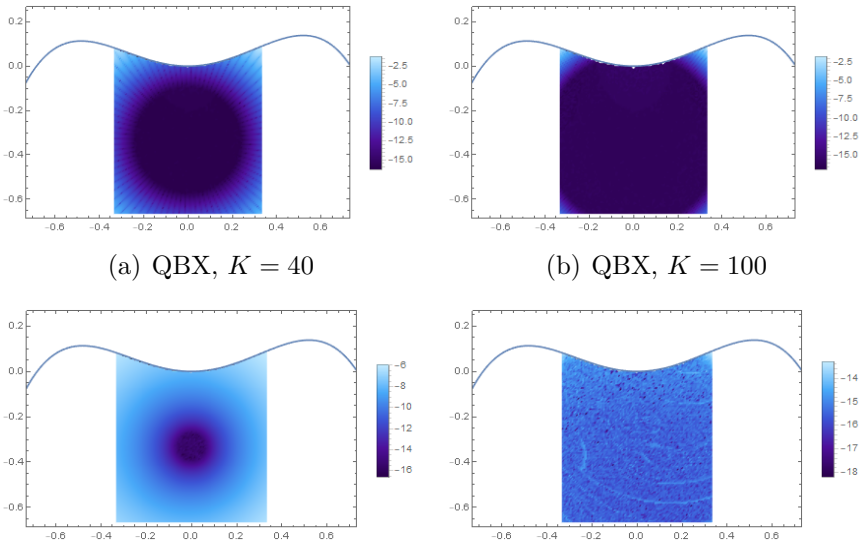

(a) QBX, $K = 40$ (b) QBX, $K = 100$

(c) QB2X, $K = 10$ (d) QB2X, $K = 30$

Figure 1: Approximation errors of the QBX and QB2X methods for different K values. The plot legends are $\log_{10}(Error)$

For the same settings, the errors from the new QB2X method are bounded by the theoretical results from standard FMM analysis (also see Fig. 13), and one can use a single QB2X representation to achieve machine precision accuracy in the entire leaf box when $K \approx 40$.

To be fair, the new QB2X method also requires a plane wave type expansion. However, for the same accuracy requirement, the additional work allows higher order boundary descriptions, much larger leaf box sizes, and a discretization strategy only based on the local properties of the density function and geometry. The new QB2X method will improve the overall algorithm efficiency, especially on parallel computers when the local operations are highly parallelizable.

Quadrature by Two Expansions: Evaluating Laplace Layer Potentials using Complex Polynomial and Plane Wave Expansions

Lingyun Ding[a], Jingfang Huang[a,*], Jeremy L. Marzuola[a], Zhuochao Tang[a]

[a]*Department of Mathematics, the University of North Carolina at Chapel Hill*

Abstract

The recently developed quadrature by expansion (QBX) technique [24] accurately evaluates the layer potentials with singular, weakly or nearly singular, or even hyper singular kernels in the integral equation reformulations of partial differential equations. The idea is to form a local complex polynomial or partial wave expansion centered at a point away from the boundary to avoid the singularity in the integrand, and then extrapolate the expansion at points near or even exactly on the boundary. In this paper, in addition to the local complex Taylor polynomial expansion, we derive new representations of the Laplace layer potentials using both the local complex polynomial and plane wave type expansions. Unlike in the QBX, the local complex polynomial expansion in the new quadrature by two expansions (QB2X) method only collects the far-field contributions and its number of expansion terms can be analyzed using tools from the classical fast multipole method (FMM). The plane wave type expansion in the QB2X method is derived by first applying the Fourier extension technique to the density and polynomial approximation of the boundary geometry, and then analytically evaluating the integral using the Residue Theorem with properly chosen complex contour. The plane wave type expansion accurately captures the high frequency properties of the layer potential that are determined (up to a prescribed accuracy) only by the local features of the density function and boundary geometry, and the nonlinear

*Corresponding author

Email addresses: dingly@live.unc.edu (Lingyun Ding), huang@email.unc.edu (Jingfang Huang), marzuola@email.unc.edu (Jeremy L. Marzuola), zctang@email.unc.edu (Zhuochao Tang)

impact of the boundary on the layer potential becomes explicit. The QB2X technique allows high order numerical discretizations and can be adopted easily in existing FMM based fast integral equation solvers. We present preliminary numerical results to validate our analysis and demonstrate the accuracy and efficiency of the QB2X representations when compared with the classical QBX method.

Keywords: Layer Potential, Quadrature by Expansion, Partial Wave Expansion, Plane Wave Expansion, Fourier Extension, Residue Theorem, Integral Equation
2010 MSC: 31C05, 32A55, 41A10, 42A10, 65D30, 65E05, 65R20, 65T40

---

1. Introduction

When the integral equation method is applied to solve a given partial differential equation, one numerical challenge is the accurate and efficient evaluation of the singular, weakly singular, or hyper singular integrals representing different potentials in the integral equation reformulations. For example, the solutions of a homogeneous elliptic equation (e.g., Laplace, Helmholtz, or Yukawa equations) with different types of boundary conditions are often re-expressed as combinations of the single layer and double layer potentials with density functions $\rho(z)$ and $\mu(z)$

$$\begin{aligned} S\rho(w) &= \int_{\Gamma} G(w,z)\rho(z)\mathrm{d}z, \\ D\mu(w) &= \int_{\Gamma} \frac{\partial G}{\partial \mathbf{n}_z}(w,z)\mu(z)\mathrm{d}z, \end{aligned} \tag{1}$$

where G is the free-space Green's function for the underlying elliptic PDE, z is the source point located on the boundary Γ, w is any target point located in the computational domain, and $\mathbf{n}_z$ is the outward normal vector at $z \in \Gamma$. The Green's function $G(w,z)$ is usually a smooth function when w is away from z on the boundary Γ, but becomes singular when $w \to z$. Therefore, different numerical strategies have to be designed for cases when w is far away from the boundary, exactly on the boundary, and close to the boundary.

The research topics of developing different numerical integration schemes for evaluating the layer potentials at a particular point w for different cases have been extensively studied. When w is far away from the boundary, classical Newton-Cotes or Gaussian quadratures for a general smooth integrand

can be applied; when w is located on the boundary, special quadrature rules can be designed, for example, the trapezoidal rule with end-point corrections in [1, 2, 23, 27, 31] or the generalized Gauss quadrature rules in [6, 7, 32]; and when w is close to the boundary, existing techniques include the change of variables to remove the principal singularity and the regularized kernel and corrections using asymptotic analysis [4, 9, 15, 20]. We particularly mention the pioneering work in [21] which applies the Barycentric Lagrange polynomial interpolation formula to derive a globally compensated spectrally accurate quadrature rule for evaluation at points close to the boundary (also see [3]); and the pioneering "quadrature by expansion" (QBX) scheme in [24] which derives a partial wave (harmonics) expansion valid in a region close to (or even containing points on) the boundary. The QBX scheme has been combined with the fast multipole method (FMM) in [30] for solving the integral equation reformulation of PDEs.

In this paper, we introduce new representations of the Laplace layer potentials that are valid in the entire leaf (childless) box in the FMM hierarchical tree structure. As the representation can be evaluated at any point in the box, the numerical scheme also belongs to the class of "quadrature by expansion" (QBX) schemes to evaluate the layer potential integrals. In Fig. 2, the leaf boxes in a uniform FMM tree with 4 levels are categorized into three groups: The green boxes are well separated from the boundary source points, from established fast multipole method (FMM) theory [17, 18], the layer potential at each target point in the box can be represented by a complex Taylor polynomial expansion which is referred to as the local expansion of the green box in the FMM algorithm. Both the red and yellow boxes are not well separated from the boundary, and each of the red boxes contains target points located both inside and outside the boundary, hence two separate solution representations become necessary, one for the interior and one for the exterior. For the red and yellow boxes, contributions from the well-separated curved boundary segments of the layer potential can still be represented using the complex local Taylor polynomial expansion, which can be efficiently computed using the FMM through the upward and downward passes for the "far-field" contributions of the sources. The numerical difficulty is the accurate representation and efficient evaluation of the near-field source contributions.

Using both the complex local Taylor polynomials and plane wave (exponential) functions in the basis, we propose a new representation of the $2D$ layer potential in this paper for the red and yellow boxes due to the near-field

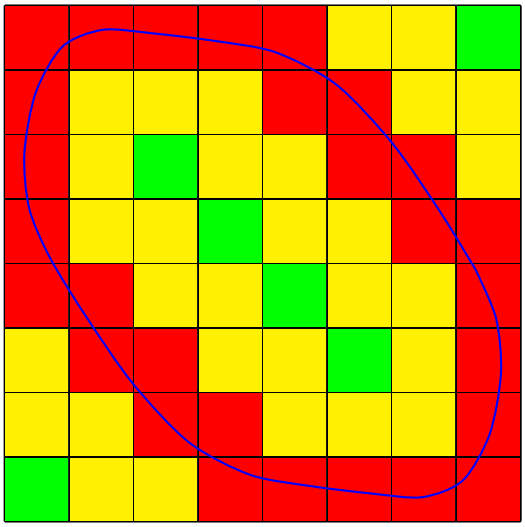

Figure 2: Different expansions for the leaf boxes in a uniform FMM hierarchical tree structure. Green: complex polynomial expansion; Yellow: one QB2X for the leaf node; Red: two QB2X required, one for the interior and one for the exterior.

layer potential source contributions. Combining both the far-field and near-field (local) density contributions, the main contribution of this paper is that the Laplace layer potentials inside each $2D$ leaf box of the FMM hierarchical tree structure can be represented as the sum of two expansions

$$\sum_{k=0}^{K} c_k (w - w_0)^k + \left(\sum_{\Im(\tilde{w}_j)>0} \sum_{p=0}^{P} \omega_p \frac{e^{\lambda_p \tilde{w}_j}}{1 + \mathrm{i}s'(\tilde{w}_j)} + \sum_{\Im(\tilde{w}_j)<0} \sum_{p=-P}^{-1} \omega_p \frac{e^{\lambda_p \tilde{w}_j}}{1 + \mathrm{i}s'(\tilde{w}_j)} \right). \tag{2}$$

Here, $w = x + \mathrm{i}y$ is a target point in the leaf box centered at w_0, the boundary is described by $z = \tilde{x} + \mathrm{i}s(\tilde{x})$, $\{\tilde{w}_j\}$ is the set of the roots of the degree J polynomial equation $z + \mathrm{i}s(z) - w = 0$ when w is inside either the red or yellow boxes (assuming $s(0) = s'(0) = 0$ after proper translations and rotations), c_k and ω_p are the complex coefficients of the polynomial and plane wave type expansions, respectively, the complex number λ_p is referred to as the node for the exponential (plane wave) expansion, $\Im(\tilde{w}_j) > 0$ and $\Im(\tilde{w}_j) < 0$ are respectively the roots on the upper half and lower half complex plane, K and P are respectively the numbers of terms in the local Taylor polynomial and plane wave expansions (no exponential expansion for a green box), and

when a root $\tilde{w}_j$ is a multiple root, the exponential type summations in the formula are considered in the limit sense involving higher order derivatives of the density function as in the classical Residue Theorem.

The local complex polynomial expansion only collects the far-field contributions and its number of expansion terms K can be analyzed using the established error analysis from the classical fast multipole method ($K = 9$, 18, 27, and 36 for 3, 6, 9, and 12 digits accuracy, respectively). The plane wave type expansion is derived by first applying the Fourier extension technique to the density function and polynomial approximation of the boundary geometry, then analytically utilizing the Residue Theorem for properly chose complex contour integrals for optimal numerical stability. The number of terms P is the same as the number of terms required in the Fourier extensions. Note that two different types of basis functions are used in the representation of the layer potential, hence we refer to our approach as the quadrature by two expansions (QB2X). In harmonic analysis, the redundant basis functions form a frame [10, 14]. Compared with classical QBX, the QB2X representation of the layer potential is valid in a much larger region and allows easier analysis of the error and its dependency on the numbers of expansion terms. Another nice feature of the new representation is that the nonlinear impact of the boundary on the layer potential becomes explicit in Eq. (2), providing an analytical tool useful for other applications. For example, Eq. (2) demonstrates that up to a prescribed error tolerance, the high frequency features of the layer potential is determined only by the local properties of the density and boundary geometry functions.

We organize this paper as follows. In Sec. 2, we review the classical QBX and the well-established Fourier extension technique which form the foundation of the QB2X technique. In Sec. 3, we derive the new representations for the single and double layer potentials in the red and yellow boxes using both the complex Taylor polynomial and plane wave basis functions. In Sec. 4, we present preliminary numerical experiments to validate our analysis and demonstrate the accuracy and efficiency of the QB2X representations when compared with the classical QBX method. Finally in Sec. 5, we summarize our results and discuss our current work to generalize QB2X to layer potentials for other types of equations in both two and three dimensions.

2. Preliminaries

The new quadrature by two expansions (QB2X) technique uses two different basis functions, the complex polynomial expansion (also referred to as the local expansion in the fast multipole method) and the plane wave type expansion using exponential functions. In this section, we present (a) the original QBX [24] which introduces the complex polynomial expansion (or partial waves for the Helmholtz and Yukawa equations) to evaluate layer potentials and (b) the Fourier extension technique [5, 8, 22] which will provide explicit formulas for the plane wave type expansion in the new QB2X technique.

2.1. Quadrature by Expansion: Evaluating Layer Potential Using Complex Polynomial Expansion

Assuming both the density function and boundary curve are sufficiently smooth, to evaluate the singular, near-singular, or hyper-singular layer potentials, in [24], it was observed that the layer potentials are smooth functions on either side of the boundary, and the integrand singularity is only associated with the non-smoothness across the boundary. Therefore the polynomial expansion of the Laplace layer potential centered at a point either in the interior or exterior of the boundary is valid at least locally. In Fig. 3, we consider a Laplace layer potential explicitly given by $\Re\left(e^{\mathrm{i}5z}\right) = \Re\left(e^{\mathrm{i}5(x+\mathrm{i}y)}\right)$ in a box $0 < x, y < 1$ where $z = x + \mathrm{i}y$ is the complex variable. The box contains part of the boundary given by the equation $\tilde{y} = s(\tilde{x}) = \frac{1}{3}(\tilde{x} - \frac{1}{2})^2$. We assume the polynomial expansion is in the form $\Re\left(\sum_{k=0}^{K} c_k (w - w_0)^k\right)$ centered at $w_0 = \frac{1}{2} + \frac{1}{3}\mathrm{i}$. We neglect the numerical errors when evaluating the expansion coefficients, i.e., the coefficients are derived exactly. In (a), we plot the analytical layer potential. In (b) and (c), we present the polynomial approximation of the layer potential using $K = 5$ and $K = 15$ terms in the expansion, and in (d), (e), and (f), we plot the $\log_{10}$ errors of the representation when $K = 5$, $K = 15$, and $K = 25$, respectively. Clearly, when the number of expansion terms K increases, the error decreases and the representation becomes valid in a much larger region.

Using standard error analysis from the FMM theory for the well separated green boxes in Fig. 2, assuming the coefficients are computed accurately, the local expansion in the form $\Re\left(\sum_{k=0}^{K} c_k (w - w_0)^k\right)$ can achieve 6-digits accuracy when K is approximately 18 and 12-digits accuracy when $K =$

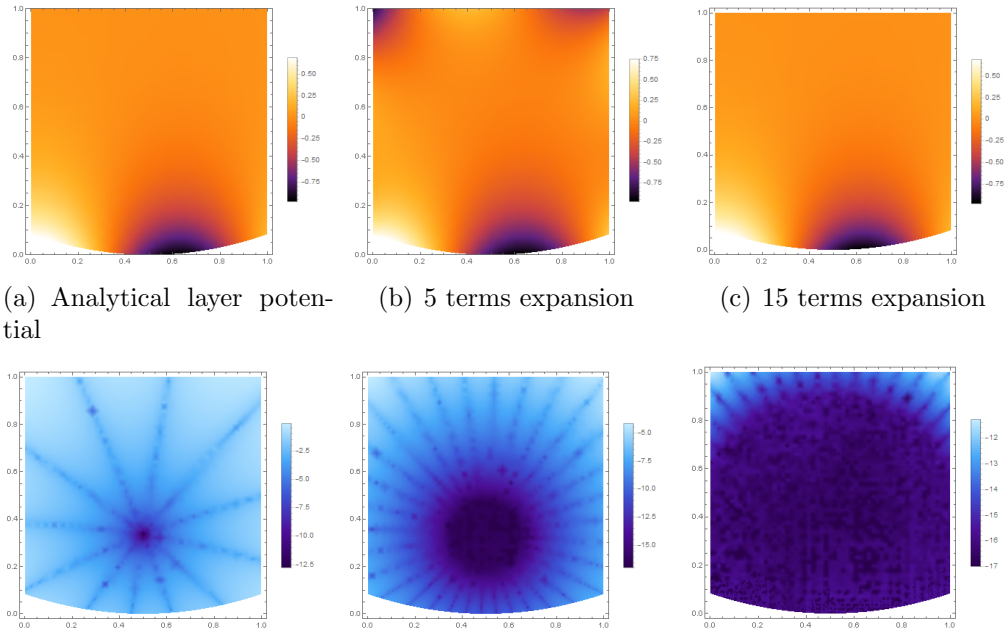

(a) Analytical layer potential (b) 5 terms expansion (c) 15 terms expansion

(d) 5 terms error (e) 15 terms error (f) 25 terms error

Figure 3: An implementation of QBX. (a): Analytical layer potential. (b) and (c): approximation using $K = 5$ and $K = 15$ terms, respectively. (d), (e), and (f): $\log_{10}$ errors for $K = 5$, $K = 15$, and $K = 25$.

36. The task of evaluating the layer potentials at points in the red and yellow boxes becomes more complicated. In [24], the choice of the local complex polynomial expansion center, the degree of the polynomial, and the quadrature schemes for computing the expansion coefficients are numerically studied to provide guidelines for parameter selection. In [16], estimates for the rate of convergence of these local expansions are derived, which can be used to analyze the approximation error of the local Taylor expansions in a leaf box. In existing FMM+QBX implementation [30], for evaluation points in one leaf node, several complex polynomial expansions may have to be formed with different expansion centers and degrees, unless the FMM hierarchical tree oversamples the density and boundary geometry. We also mention that in existing QBX implementations, the boundary description $(x, s(x))$ does not explicitly appear in the formulas. This will be addressed in the new QB2X method in Sec. 3.

2.2. Fourier Extension: Approximation Using Exponentials

Compared with a polynomial basis, the exponential expansions, if it can be derived accurately and efficiently, may show better numerical properties in efficiency. One example is the translations in the FMM algorithms. When the exponential (plane wave) expansions are used, the translations become diagonal and the number of operations is reduced from the polynomial expansion's $O(K^2)$ to the plane wave expansion's $O(K)$ when K terms are used in both expansions [11, 12, 19]. Unfortunately, deriving the optimal exponential expansion for a general function requires nonlinear optimization, and the uniqueness of the solution is not guaranteed. However, in some particular cases, a good exponential expansion approximation can be derived. For example, when the function is smooth and periodic, then the Fourier series can be computed efficiently and the expansion converges rapidly. Another example is when the inverse integral transform of the function is available, then the exponential expansion problem becomes an integration problem, and the weights and nodes of the exponential expansions can be computed using the generalized Gauss quadrature method [26, 32]. Using the Fourier series to approximate a non-periodic function is also a well-studied topic. Consider a non-periodic function f on $[-1, 1]$, applying the Fourier extension technique, a suitable periodic function g on a larger domain $[-T, T]$ $(T > 1)$ is computed stably, so the Fourier series expansion of g matches f on the interval $[-1, 1]$, see [5, 8, 22] and references therein. We have implemented the scheme in [22], which solves the least square optimization problem to compute an ac-

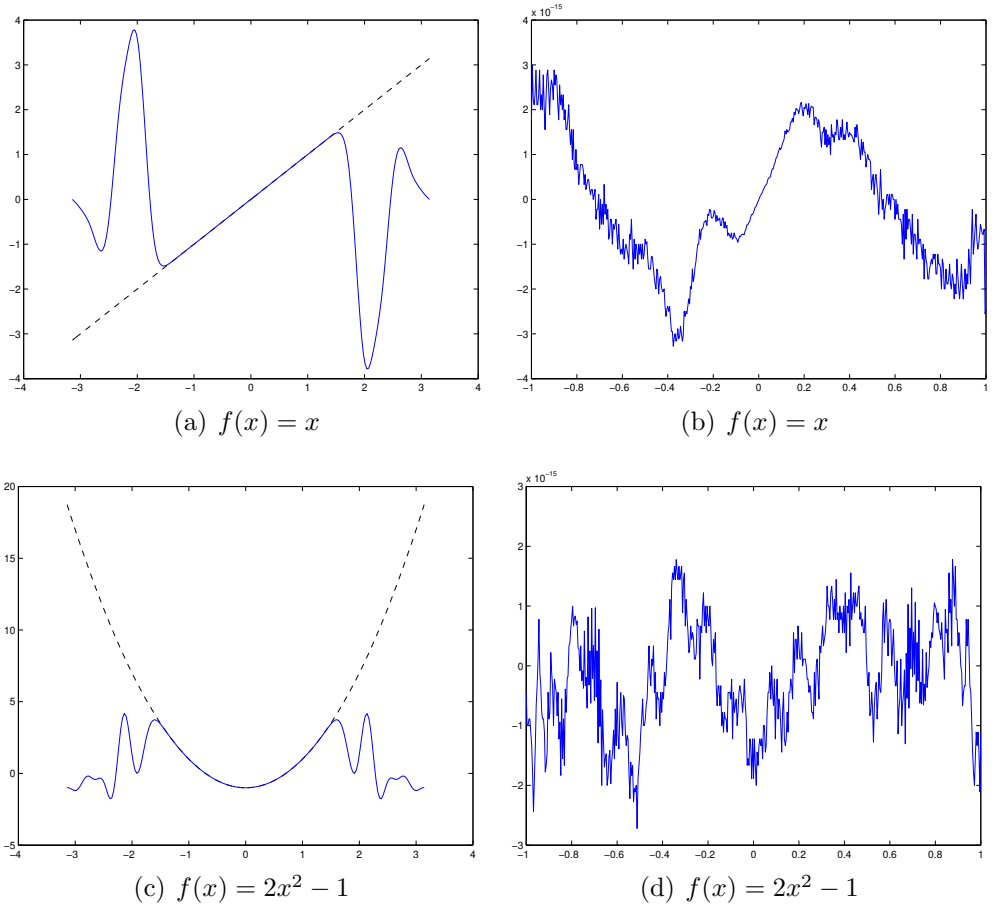

(a) $f(x) = x$ (b) $f(x) = x$

(c) $f(x) = 2x^2 - 1$ (d) $f(x) = 2x^2 - 1$

Figure 4: (a) and (c): Fourier extension $g(x) = \sum_{p=-P}^{P} c_p e^{\mathrm{i}px}$ (solid line) of the given function f (dashed line), $P = 30$. (b) and (d): approximation errors on $[-1, 1]$.

curate Fourier series representation of a smooth function defined on $[-1,1]$. In Fig. 4, we present the computed Fourier series with fundamental period 2π for the two Chebyshev basis polynomials $T_1(x) = x$ and $T_2(x) = 2x^2 - 1$. The Fourier series approximation on $[-1,1]$ achieves machine precision accuracy for both cases. Using the Fourier extension technique, a translation matrix can be precomputed to map the commonly used Chebyshev or other orthogonal polynomial basis functions to the Fourier basis functions that are periodic in a larger domain.

3. Quadrature by Two Expansions: Combining Complex Polynomial and Plane Wave Expansions

3.1. Problem Setup

As all the far-field layer potential density contributions can be accurately and efficiently computed using the fast multipole method, in this section, we focus on the near-field (local) density contributions to the red and yellow boxes in Fig. 2. Consider a target point $w = x + iy$ in one of the red or yellow boxes. We assume the boundary is parametrically described by $z = \tilde{x} + \mathrm{i}s(\tilde{x}), -1 \leq \tilde{x} \leq 1$ and $s(0) = 0, s'(0) = 0$ after proper scaling, translation, and rotation as in Fig. 5. One of the yellow leaf boxes is shown and we assume the two end points $(-1, s(-1))$ and $(1, s(1))$ are well-separated from this leaf box with center w_0. We assume both the density function $\rho(\tilde{x})$ and boundary $s(\tilde{x})$ are well approximated by some expansion representations for $-1 \leq \tilde{x} \leq 1$. In previous work in [30], polynomial expansions are used and the degree of the polynomials to approximate $s(\tilde{x})$ is usually chosen to be less than that of $\rho(\tilde{x})$. Next, we present the detailed representation formulas for the single and double layer potentials

$$\begin{aligned} S\rho(w) = &\int_{-1}^{1} G(w,z)\rho(\tilde{x})|z'(\tilde{x})|\mathrm{d}\tilde{x}, \\ D\rho(w) = &\int_{-1}^{1} \frac{\partial G}{\partial \mathbf{n}_z}(w,z)\rho(\tilde{x})|z'(\tilde{x})|\mathrm{d}\tilde{x} \end{aligned} \tag{3}$$

where $w = x + \mathrm{i}y$ is the target point in the yellow or red leaf box, $z = \tilde{x} + \mathrm{i}s(\tilde{x})$ is the source on the boundary, and $|z'(\tilde{x})| = \sqrt{1 + s'(\tilde{x})^2}$.

3.2. Laplace Layer Potentials as Complex Contour Integrals

We start from the double layer potential to avoid the branch cut analysis of the log function in the kernel. To evaluate the double layer potential at the target point $w = x + \mathrm{i}y$ in a yellow or red leaf box, the contribution from the

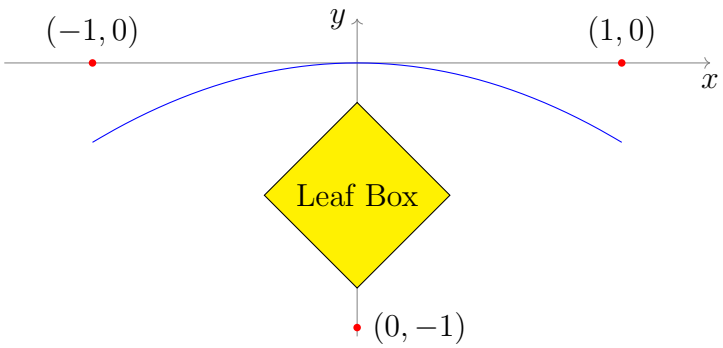

Figure 5: A leaf box close to the boundary.

source density function $\rho(\tilde{x})$ defined on the boundary segment $z = \tilde{x} + \mathrm{i}s(\tilde{x})$, $-1 \le \tilde{x} \le 1$, becomes

$$\begin{aligned} DLP(w = x + iy) = & \int_{-1}^{1} \frac{\partial G(w,z)}{\partial \mathbf{n}_z} \rho(\tilde{x}) \, |z'(\tilde{x})| \, \mathrm{d}\tilde{x} \\ = & \frac{1}{2\pi} \int_{-1}^{1} \frac{\langle x-\tilde{x}, y-s(\tilde{x})\rangle}{(x-\tilde{x})^2+(y-s(\tilde{x}))^2} \cdot \frac{\langle s'(\tilde{x}), -1\rangle}{\sqrt{1+s'(\tilde{x})^2}} \rho(\tilde{x}) \sqrt{1+s'(\tilde{x})^2} \mathrm{d}\tilde{x} \\ = & \frac{1}{2\pi} \int_{-1}^{1} \frac{(x-\tilde{x})s'(\tilde{x}) - (y-s(\tilde{x}))}{(x-\tilde{x})^2+(y-s(\tilde{x}))^2} \rho(\tilde{x}) \mathrm{d}\tilde{x} \end{aligned} \tag{4}$$

where $\frac{\partial G}{\partial \mathbf{n}_z} = \frac{1}{2\pi} \frac{w-z}{\|w-z\|} \cdot \mathbf{n}_z(\tilde{x})$, $\mathbf{n}_z(\tilde{x}) = \frac{\langle s'(\tilde{x}), -1\rangle}{\sqrt{1+s'(\tilde{x})^2}}$. In order to apply the complex contour integral theory and Residue Theorem, using

$$\frac{1}{w-z} = \frac{\overline{w-z}}{(w-z)\overline{(w-z)}} = \frac{(x-\tilde{x}) - \mathrm{i}(y-s(\tilde{x}))}{(x-\tilde{x})^2 + (y-s(\tilde{x}))^2},$$

we get

$$\begin{aligned} \Re\left(\frac{1}{w-z} s'(\tilde{x})\right) &= \frac{(x-\tilde{x})s'(\tilde{x})}{(x-\tilde{x})^2 + (y-s(\tilde{x}))^2}, \\ \Im\left(\frac{1}{w-z}\right) &= \frac{-(y-s(\tilde{x}))}{(x-\tilde{x})^2 + (y-s(\tilde{x}))^2}. \end{aligned}$$

The double layer potential becomes the sum of the complex contour integrals

$$\begin{aligned} DLP(w) = & \frac{1}{2\pi}\int_{-1}^{1} \Re(\frac{1}{w-z})s'(\tilde{x})\rho(\tilde{x})\mathrm{d}\tilde{x} + \frac{1}{2\pi}\int_{-1}^{1} \Im(\frac{1}{w-z})\rho(\tilde{x})\mathrm{d}\tilde{x} \\ = & \frac{1}{2\pi}\Re\int_{-1}^{1} \frac{s'(\tilde{x})\rho(\tilde{x})}{w-(\tilde{x}+\mathrm{i}s(\tilde{x}))}\mathrm{d}\tilde{x} + \frac{1}{2\pi}\Im\int_{-1}^{1} \frac{\rho(\tilde{x})}{w-(\tilde{x}+\mathrm{i}s(\tilde{x}))}\mathrm{d}\tilde{x}. \end{aligned} \tag{5}$$

Next we consider the single layer potential

$$\begin{aligned} SLP(w) = & \Re(\frac{1}{2\pi}\int_{-1}^{1} \log|w-z|\rho(z)\mathrm{d}z) \\ = & \Re(\frac{1}{2\pi}\int_{-1}^{1} \frac{1}{2}\log((x-\tilde{x})^2+(y-s(\tilde{x}))^2)\rho(\tilde{x})\left|1+\mathrm{i}s'(\tilde{x})\right|\mathrm{d}\tilde{x}) \\ = & \frac{1}{2\pi}\int_{-1}^{1} \frac{1}{2}\log((x-\tilde{x})^2+(y-s(\tilde{x}))^2)\tilde{\rho}(\tilde{x})\mathrm{d}\tilde{x} \end{aligned} \tag{6}$$

where $\tilde{\rho}(\tilde{x}) = \rho(\tilde{x})\left|1+\mathrm{i}s'(\tilde{x})\right|$. We apply the integration by parts to avoid the discussions of the branch cut in the kernel function as follows: We first use the Fourier extension technique to represent the real function $\tilde{\rho}(\tilde{x})$ as $\tilde{\rho}(\tilde{x}) = \sum_{p=-P}^{P} \omega_p e^{\mathrm{i}p\tilde{x}}$, and define

$$f(\tilde{x}) = \sum_{p=-P,p\neq 0}^{P} \frac{\omega_p}{\mathrm{i}p}e^{\mathrm{i}p\tilde{x}} + \omega_0\tilde{x},$$

which is a particular anti-derivative of $\tilde{\rho}(\tilde{x})$ as $f'(\tilde{x}) = \tilde{\rho}(\tilde{x})$. Using f we have

$$\begin{aligned} SLP(w) = & \frac{1}{2\pi}\int_{-1}^{1} \frac{1}{2}\log((x-\tilde{x})^2+(y-s(\tilde{x}))^2)\mathrm{d}f(\tilde{x}) \\ = & \frac{1}{2\pi}\frac{1}{2}\log((x-\tilde{x})^2+(y-s(\tilde{x}))^2)f(\tilde{x})|_{-1}^{1} \\ & + \frac{1}{2\pi}\int_{-1}^{1} f(\tilde{x})\frac{(x-\tilde{x})+(y-s(\tilde{x}))s'(\tilde{x})}{(x-\tilde{x})^2+(y-s(\tilde{x}))^2}\mathrm{d}\tilde{x} \\ = & I_1 + I_2. \end{aligned} \tag{7}$$

The I_1 term can be evaluated directly or translated into a local expansion as both end points are well-separated from the leaf box containing $w = x + \mathrm{i}y$. For I_2, simple algebra shows that

$$\begin{aligned} I_2 = & \frac{1}{2\pi}\int_{-1}^{1} f(\tilde{x})\frac{(x-\tilde{x})}{(x-\tilde{x})^2+(y-s(\tilde{x}))^2}\mathrm{d}\tilde{x} + \frac{1}{2\pi}\int_{-1}^{1} f(\tilde{x})\frac{(y-s(\tilde{x}))s'(\tilde{x})}{(x-\tilde{x})^2+(y-s(\tilde{x}))^2}\mathrm{d}\tilde{x} \\ = & \frac{1}{2\pi}\Re\int_{-1}^{1} (\frac{1}{w-(\tilde{x}+\mathrm{i}s(\tilde{x}))})f(\tilde{x})\mathrm{d}\tilde{x} - \frac{1}{2\pi}\Im\int_{-1}^{1} (\frac{1}{w-(\tilde{x}+\mathrm{i}s(\tilde{x}))})s'(\tilde{x})f(\tilde{x})\mathrm{d}\tilde{x}. \end{aligned} \tag{8}$$

In summary, the Laplace layer potentials can be represented as combinations of different complex contour integrals. We therefore focus on the complex integral

$$\int_{-1}^{1} \frac{f(\tilde{x})}{(\tilde{x} + \mathrm{i}s(\tilde{x})) - w} \mathrm{d}\tilde{x}. \tag{9}$$

3.3. Explaining QB2X using Straight Line Boundary ($s(\tilde{x}) = 0$)

We present the ideas of the QB2X method using the case when $s(\tilde{x}) = 0$ to simplify the discussions and formulas, i.e., z is on the straight line segment connecting $(-1, 0)$ and $(1, 0)$. In this case, Eq. (9) becomes

$$\int_{-1}^{1} \frac{f(z)}{z - w} \mathrm{d}z.$$

As $f(z)$ is a function defined on the real line segment, the Fourier extension technique can be applied directly or using the precomputed translation operator from the polynomial basis to the Fourier series to derive

$$f(z) \approx \sum_{p=-P}^{P} \omega_p e^{\mathrm{i}pz}$$

and Eq. (9) becomes

$$\begin{aligned} \int_{-1}^{1} \tfrac{f(z)}{z-w} \mathrm{d}z &\approx \int_{-1}^{1} \tfrac{1}{z-w} \Big(\sum_{p=-P}^{P} \omega_p e^{\mathrm{i}pz} \Big) \mathrm{d}z \\ &= \int_{-1}^{1} \sum_{p=0}^{P} \tfrac{1}{z-w} \omega_p e^{\mathrm{i}pz} \mathrm{d}z + \int_{-1}^{1} \sum_{p=-P}^{-1} \tfrac{1}{z-w} \omega_p e^{\mathrm{i}pz} \mathrm{d}z \\ &= I_1 + I_2, \end{aligned} \tag{10}$$

where I_1 only contains the non-negative p frequencies and I_2 contains the negative ones.

We first study I_1 as a portion of the contour integral

$$\sum_{p=0}^{P} \int_{C} \frac{1}{z - w} \omega_p e^{\mathrm{i}pz} \mathrm{d}z$$

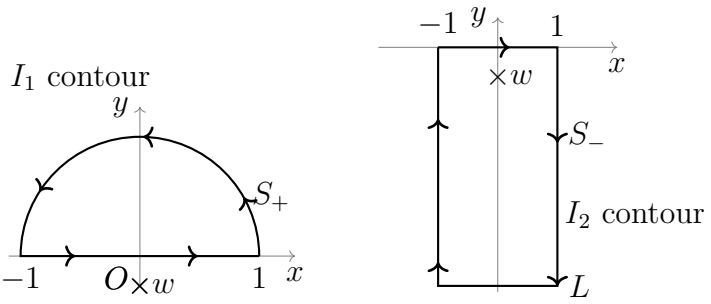

Figure 6: The upper (left) and lower (right) contours for I_1 and I_2, respectively.

where a sample contour C is shown in the left plot of Fig. 6. It consists of the line segment from -1 to 1 and the semi-circle (denoted by S_+) on the upper half plane. As the integrand is analytic inside the contour and the pole is located at w outside the contour, by the Residue Theorem, we have

$$\sum_{p=0}^{P} \int_C \frac{1}{z-w} \omega_p e^{\mathrm{i}pz} \mathrm{d}z = 0.$$

Consequently,

$$I_1 = \int_{-1}^{1} \sum_{p=0}^{P} \frac{1}{z-w} \omega_p e^{\mathrm{i}pz} \mathrm{d}z = -\sum_{p=0}^{P} \int_{S_+} \frac{1}{z-w} \omega_p e^{\mathrm{i}pz} \mathrm{d}z. \tag{11}$$

Unlike the line segment from -1 to 1, the semi-circle S_+ is well-separated from the leaf box containing w and the contribution from the density defined on the semi-circle can be collected into a local expansion as in

$$\begin{aligned} I_1 = & -\sum_{p=0}^{P} \int_{S_+} \frac{1}{(z-w_0)-(w-w_0)} \omega_p e^{\mathrm{i}pz} \mathrm{d}z = -\sum_{p=0}^{P} \int_{S_+} \frac{1}{(z-w_0)(1-\frac{w-w_0}{z-w_0})} \omega_p e^{\mathrm{i}pz} \mathrm{d}z \\ \approx & -\sum_{p=0}^{P} \int_{S_+} \frac{1}{(z-w_0)} \sum_{k=0}^{K} (\tfrac{w-w_0}{z-w_0})^k \omega_p e^{\mathrm{i}pz} \mathrm{d}z = -\sum_{k=0}^{K} c_k (w-w_0)^k \end{aligned} \tag{12}$$

where w_0 is the center of the leaf box, $c_k = \left(\sum_{p=0}^{P} \omega_p \int_{S_+} \frac{e^{\mathrm{i}pz}}{(z-w_0)^{k+1}} \mathrm{d}z \right)$ are the local expansion coefficients and the number of terms K is controlled by the decay rate of $|(\frac{w-w_0}{z-w_0})^k|$ which can be easily estimated for the given contour and target leaf box following the standard fast multipole method analysis. Introducing $r_{max} = max_{\{z \in S_+, w \in \text{leaf box}\}} |\frac{w-w_0}{z-w_0}|$ and noting that when p is non-negative, $|e^{ipz}|$ decreases when z on the contour moves away from the real axis, a very loose estimate of the truncation error is given by

$$\text{Truncation Error} \leq c \left(\sum_{p=0}^{P} |\omega_p| \right) r_{max}^{K+1}$$

for some constant c. Since in the current analysis $s(\tilde{x}) = 0$, it is straightforward to verify that $K = 9$, 18, 27, and 36 will provide results with at least 3, 6, 9, and 12 accurate digits, respectively. Also, the numerical stability issues associated with exponentially growing $|e^{ipz}|$ values can be avoided and the local expansion coefficients can be computed accurately using standard quadrature rules. Therefore, the non-negative modes can be represented as a local complex Taylor polynomial expansion. Unfortunately, the negative p frequencies cannot be computed using this contour, as the function e^{ipz} grows exponentially when z on the contour moves away from the real axis for $p < 0$.

To compute I_2, a different contour C on the lower half complex plane has to be chosen, a sample contour is shown on the right plot of Fig. 6. It consists of a rectangle with one side being the line segment from -1 to 1, and a sufficiently large (can be ∞) constant L is introduced to determine the length of the other side. We denote the part of the contour consisting of the three other sides of the rectangle by S_-. Note that e^{ipz} decays exponentially when z on S moves away from the real axis for $p < 0$. As w is inside the contour, applying the Residue Theorem, for each negative frequency p, we have

$$\int_{-1}^{1} \frac{1}{z-w} \omega_p e^{\mathrm{i}pz} \mathrm{d}z + \int_{S_-} \frac{1}{z-w} \omega_p e^{\mathrm{i}pz} \mathrm{d}z = -2\pi \mathrm{i} Res[\frac{1}{z-w} \omega_p e^{\mathrm{i}pz}, w].$$

Therefore, we can compute I_2 using

$$\begin{aligned} I_2 = & \int_{-1}^{1} \sum_{p=-P}^{-1} \frac{1}{z-w}\omega_p e^{\mathrm{i}pz}\mathrm{d}z \\ = & -2\pi\mathrm{i}Res[\sum_{p=-P}^{-1} \frac{1}{z-w}\omega_p e^{\mathrm{i}pz}, w] - \int_{S_-} \sum_{p=-P}^{-1} \frac{1}{z-w}\omega_p e^{\mathrm{i}pz}\mathrm{d}z \\ = & -2\pi\mathrm{i} \sum_{p=-P}^{-1} \omega_p e^{\mathrm{i}pw} - \int_{S} \sum_{p=-P}^{-1} \frac{1}{z-w}\omega_p e^{\mathrm{i}pz}\mathrm{d}z \\ \approx & -2\pi\mathrm{i} \sum_{p=-P}^{-1} \omega_p e^{\mathrm{i}pw} - \sum_{k=0}^{K} c_k (w-w_0)^k \end{aligned} \tag{13}$$

where the local expansion (second summation in the formula) coefficients are given by

$$c_k = \sum_{p=-P}^{-1} \omega_p \int_{S_-} \frac{e^{\mathrm{i}pz}}{(z-w_0)^{k+1}}\mathrm{d}z$$

which are derived using the same separation of variables as in I_1. As the leaf box is well-separated from S_-, the number K in the local polynomial expansion can be determined using the same FMM error analysis as in I_1 and we skip the details.

Combining I_1, I_2, and the far-field density contributions for this special case, we conclude that the Laplace layer potential in the leaf box can be represented as a combination of the local complex Taylor polynomial expansion and plane wave type expansion as in Eq. (2). The number of terms in the local polynomial expansion is determined by standard FMM error analysis as all the involved contributions are well-separated from the leaf box. The number of terms in the plane wave type expansion is the same as that in the Fourier extension of the density and boundary functions for $-1 < \tilde{x} < 1$.

Comment on r_{max}: Smaller r_{max} values are possible by including a larger portion of the boundary when computing I_1 and I_2, e.g., by also including contributions from the second nearest neighbors [28], at the cost of more terms in the Fourier extension. The balance of the numbers of terms P in the exponential expansion and K in the polynomial expansion is related with the optimal discretization strategies when generating the FMM adaptive tree, which is currently being investigated.

Comment on the contours: We mention that the choice of the contour is not unique. Other contours can also be used. However changing the

contours will not change the values of the expansion coefficients. It will only change the accuracy and efficiency of the numerical integration scheme for computing these values and the estimated number K for truncating the local Taylor expansion. Our numerical experiments in Sec. 4 show that the current choice for straight line boundary allows accurate and efficient computations of these coefficients and provides acceptable bounds for K. In the next section, we discuss a very practical contour selection for general geometry settings.

3.4. Numerically Stable QB2X for general geometry

Next we add the role of the boundary geometry in the frame representation of $\int_{-1}^{1} \frac{f(\tilde{x})}{(\tilde{x}+\mathrm{i}s(\tilde{x}))-w}\mathrm{d}\tilde{x}$. We assume $s(\tilde{x}) \neq 0$ is a polynomial of $\tilde{x}$, $s(\tilde{x}) = s'(\tilde{x}) = 0$ at $\tilde{x} = 0$, and $s(\tilde{x})$ sufficiently resolves the boundary to a prescribed accuracy. Similar to the $s(\tilde{x}) = 0$ case, we replace $f(z)$ by its Fourier series expansion which can be computed using the Fourier extension technique, and separate the integral in Eq. (9) into two parts

$$\begin{aligned}
\int_{-1}^{1} \frac{f(z)}{(z+\mathrm{i}s(z))-w}\mathrm{d}z = & \int_{-1}^{1} \frac{1}{z+\mathrm{i}s(z)-w}\Big(\sum_{p=-P}^{P} \omega_p e^{\mathrm{i}pz}\Big)\mathrm{d}z \\
= & \int_{-1}^{1} \sum_{p=0}^{P} \frac{1}{z+\mathrm{i}s(z)-w}\omega_p e^{\mathrm{i}pz}\mathrm{d}z + \int_{-1}^{1} \sum_{p=-P}^{-1} \frac{1}{z+\mathrm{i}s(z)-w}\omega_p e^{\mathrm{i}pz}\mathrm{d}z \\
= & I_1 + I_2
\end{aligned} \tag{14}$$

The numerical stability of the Fourier extension methods were discussed in [5, 8, 22]. Next we present all the required building blocks to stably evaluate I_1 and I_2.

3.4.1. Roots of $z + \mathrm{i}s(z) - w = 0$

Finding all the roots $\{\tilde{w}_j\}, j = 1, \cdots, J$ of the degree J polynomial equation $z + \mathrm{i}s(z) - w = 0$ is a well studied topic. When J is less than 5, analytical formulas are available for the roots. For larger J values, eigenvalue algorithms can be applied to compute the roots. The accuracy of these roots is controlled by the condition number of the polynomial equation. However, the accuracy of the QB2X method doesn't depend on the accuracy of the roots, it only depends on how accurate the polynomial $z + \mathrm{i}s(z) - w$ can be approximated by its factorization $c(z - \tilde{w}_1)(z - \tilde{w}_2)\cdots(z - \tilde{w}_J)$ where c is the coefficient for the highest degree term. Luckily, most polynomial root finding algorithms are backward stable [13] when the error is measured by

$|(z+\mathrm{i}s(z)-w)-c(z-\tilde{w}_1)(z-\tilde{w}_2)\cdots(z-\tilde{w}_J)|$ instead of the accuracy of each root.

3.4.2. Choice of Complex Contour

To avoid the exponential growth of the Fourier terms, similar to the $s(\tilde{x})=0$ case, we use a contour in the upper half plane to stably evaluate I_1 which only contains the non-negative Fourier modes, and a contour in the lower half plane for I_2 containing all the negative Fourier modes. Consider a closed complex contour consisting of the line segment $[-1,1]$ and S representing the rest of the integration contour. Note that in order to be able to represent the contributions on S as a local expansion

$$\begin{aligned}\int_S \tfrac{1}{(z+\mathrm{i}s(z)-w_0)-(w-w_0)}\omega_p e^{\mathrm{i}pz}\mathrm{d}z &= \int_S \tfrac{1}{(z+\mathrm{i}s(z)-w_0)(1-\frac{w-w_0}{z+\mathrm{i}s(z)-w_0})}\omega_p e^{\mathrm{i}pz}\mathrm{d}z \\ \approx \int_S \tfrac{1}{(z+\mathrm{i}s(z)-w_0)}\sum_{k=0}^{K}(\tfrac{w-w_0}{z+\mathrm{i}s(z)-w_0})^k\omega_p e^{\mathrm{i}pz}\mathrm{d}z &= -\sum_{k=0}^{K} c_k(w-w_0)^k\end{aligned} \tag{15}$$

where w_0 is the center of the leaf box and $c_k=\omega_p\int_S \frac{e^{\mathrm{i}pz}}{(z+\mathrm{i}s(z)-w_0)^{k+1}}\mathrm{d}z$ are the local expansion coefficients, classical FMM error analysis requires that the ratio $|\frac{w-w_0}{z+\mathrm{i}s(z)-w_0}|\le\frac{\sqrt{2}}{3}$. This inequality is valid at the points $z=-1$ and $z=-1$. However if S is close to any of the roots of $z+\mathrm{i}s(z)-w=0$, then the max value of the ratio $|\frac{w-w_0}{z+\mathrm{i}s(z)-w_0}|$ for $z\in S$ becomes closer to 1 and huge error is expected if the expansion is truncated using standard FMM error control strategy.

As we prefer a fixed S for all w values in a leaf box, a practical choice is to use the S consisting of the line segments $(-R,-1)\cup(1,R)$ and the upper half plane semi-circle of radius R centered at the origin. We then let $R\to\infty$ so the integral on the semi-circle approaches 0. There are several interesting properties of this particular contour, including (a) the values $|x+\mathrm{i}s(x)-w|\to\infty$ when $x\to\pm\infty$; (b) when the geometry is sufficiently resolved so that $s(x)$ becomes closer to a straight line, the inequality

$$|\frac{w-w_0}{x+\mathrm{i}s(x)-w_0}|\le\frac{\sqrt{2}}{3} \tag{16}$$

holds for all points x on the two (rescaled) line segments; and (c) when the geometry data in the second nearest neighbors (or further well-separated) leaf boxes are used when constructing the approximation polynomial of the boundary geometry, it becomes more likely to satisfy the inequality in Eq. (16)

as the added interpolation data points automatically satisfy the inequality. Using the special semi-circle contour, we can leave the task of satisfying Eq. (16) to the adaptive computational domain discretization step, and assume the constructed boundary geometry polynomial approximation satisfies the constraint for each red or yellow leaf box. Note that this adaptive discretization strategy only depends on the geometry, not the smoothness of the density function or the layer potential.

The contour for I_2 uses the same line segments as that for I_1 but the lower half plane semi-circle. As the integrals for each Fourier mode on the line segments for both I_1 and I_2 are identical except for the different coefficients, therefore they only need to be computed once. This will improve the overall algorithm efficiency.

3.4.3. Quadrature by Two Expansions for General Geometry

Applying the Residue Theorem to the special contour, we can write

$$\begin{aligned} I_1 = & \int_{-1}^{1} \sum_{p=0}^{P} \frac{1}{z+\mathrm{i}s(z)-w} \omega_p e^{\mathrm{i}pz} \mathrm{d}z \\ = & -\sum_{p=0}^{P} \int_{S} \frac{1}{z+\mathrm{i}s(z)-w} \omega_p e^{\mathrm{i}pz} \mathrm{d}z - 2\pi\mathrm{i} \sum_{j=1}^{J_U} Res[\sum_{p=0}^{P} \frac{1}{z+\mathrm{i}s(z)-w} \omega_p e^{\mathrm{i}pz}, \tilde{w}_j] \\ \approx & -\sum_{k=0}^{K} c_k (w-w_0)^k - 2\pi\mathrm{i} \sum_{j=1}^{J_U} \sum_{p=0}^{P} \omega_p \frac{e^{\mathrm{i}p\tilde{w}_j}}{1+\mathrm{i}s'(\tilde{w}_j)} \end{aligned} \tag{17}$$

where J_U is the number of roots of the polynomial equation $z+\mathrm{i}s(z)-w=0$ on the upper half plane, and

$$\begin{aligned} I_2 = & \int_{-1}^{1} \sum_{p=-P}^{-1} \frac{1}{z+\mathrm{i}s(z)-w} \omega_p e^{\mathrm{i}pz} \mathrm{d}z \\ = & -\int_{S} \sum_{p=-P}^{-1} \frac{1}{z+\mathrm{i}s(z)-w} \omega_p e^{\mathrm{i}pz} \mathrm{d}z - 2\pi\mathrm{i} \sum_{j=1}^{J_L} Res[\sum_{p=-P}^{-1} \frac{1}{z+\mathrm{i}s(z)-w} \omega_p e^{\mathrm{i}pz}, \tilde{w}_j] \\ \approx & -\sum_{k=0}^{K} c_k (w-w_0)^k - 2\pi\mathrm{i} \sum_{j=1}^{J_L} \sum_{p=-P}^{-1} \omega_p \frac{e^{\mathrm{i}p\tilde{w}_j}}{1+\mathrm{i}s'(\tilde{w}_j)} \end{aligned} \tag{18}$$

where J_L is the number of roots on the lower half plane. Combining I_1 and I_2, we derive the QB2X representation in Eq. (2) which shows that the layer potential depends non-linearly on the geometry in three different ways: the additional $s'(\tilde{w})$ term in the denominator of the plane wave expansion, the nonlinear dependency when finding the root $\tilde{w}$ using the polynomial equation

$z+\mathrm{i}s(z)-w=0$, and the adaptive discretization strategy using the constraint condition in Eq. (16) which depends on the boundary geometry function $s(z)$. As all the far-field density contributions are collected in the local expansion, up to the prescribed accuracy requirement, the high frequency components of the solution are therefore determined only by the local density function and geometry.

Comment on computing c_k: The local expansion coefficients in both I_1 and I_2 are computed using the same set of values of $\int_1^{\infty} \frac{e^{\mathrm{i}pz}}{(z+\mathrm{i}s(z)-w_0)^{k+1}}\mathrm{d}z$ and $\int_{-\infty}^{-1} \frac{e^{\mathrm{i}pz}}{(z+\mathrm{i}s(z)-w_0)^{k+1}}\mathrm{d}z$. These values are currently computed using numerical quadrature rules. However, as the roots (and hence the factorization) are already available, one can find analytical formulas for evaluating these integrals utilizing the special exponential integral function $E_n(z)$ [25, 29] defined as $E_n(z) = z^{n-1}\int_z^{\infty} \frac{e^{-t}}{t^n}dt$.

3.4.4. Stably Evaluating Plane Wave Sums

The plane wave type expansion in the QB2X method comes from the Residue Theorem applied to the contour integral of the form

$$\oint \frac{g(z)}{c_0(z-\tilde{w}_1)(z-\tilde{w}_2)\cdots(z-\tilde{w}_J)}\mathrm{d}z = 2\pi\mathrm{i}\sum_{j=1}^{J}\frac{g(\tilde{w}_j)}{1+\mathrm{i}s'(\tilde{w}_j)} \tag{19}$$

where c_0 is the coefficient of the highest degree term of the polynomial $z+\mathrm{i}s(z)-w$. When the integration contour is well-separated from the roots $\{\tilde{w}_j\}$, classical numerical integration quadrature rules can be applied to directly evaluate the integral on the left of Eq. (19). When the roots become closer to the integration path, the integral becomes more singular and the summation on the right side of Eq. (19) becomes a better numerical tool if it can be evaluated accurately.

When all the roots in the set $\{\tilde{w}_j\}$ are simple and well-separated, then computing the summation $\sum_{j=1}^{J}\frac{g(\tilde{w}_j)}{1+\mathrm{i}s'(\tilde{w}_j)}$ has no numerical stability issues. However, when some of the roots are closely clustered, then the formula becomes ill-conditioned numerically. This can be explained by considering the case when two roots $\tilde{w}_1 \approx \tilde{w}_2$ are close to each other, and then the contour integral becomes

$$\frac{1}{2\pi\mathrm{i}}\oint \frac{g(z)}{(z-\tilde{w}_1)(z-\tilde{w}_2)} = \frac{g(\tilde{w}_1)}{\tilde{w}_1-\tilde{w}_2} + \frac{g(\tilde{w}_2)}{\tilde{w}_2-\tilde{w}_1} = \frac{g(\tilde{w}_2)-g(\tilde{w}_1)}{\tilde{w}_2-\tilde{w}_1}.$$

Clearly, the summation formula suffers from the same type of numerical instability as the difference approximation of the derivatives.

However, as the function $g(z)$ is in the form of a Fourier series, its derivative and higher order derivatives can be computed analytically. We therefore apply the following strategy to stably and accurately compute the summation on the right side of Eq. (19) for clustered roots. We first find a *center* $\tilde{w}_0$ of the clustered roots $\{\tilde{w}_j\}$ and assume all the other roots are well-separated from the cluster, then we Taylor expand all the $z - \tilde{w}_j$ terms as in the following formula.

$$\begin{aligned} & \oint \frac{f(z)}{(z-\tilde{w}_1)(z-\tilde{w}_2)\cdots(z-\tilde{w}_J)}\mathrm{d}z = \oint \frac{f(z)}{(z-\tilde{w}_0)^J(1-\frac{\delta_1}{z-\tilde{w}_0})(1-\frac{\delta_2}{z-\tilde{w}_0})\cdots(1-\frac{\delta_J}{z-\tilde{w}_0})}\mathrm{d}z \\ = & \oint \frac{f(z)}{(z-\tilde{w}_0)^J}(1+\frac{c_1}{z-\tilde{w}_0}+\frac{c_2}{(z-\tilde{w}_0)^2}+\cdots)\mathrm{d}z = \sum_{m=J}^{\infty} w_m f^{(m)}(\tilde{w}_0), \end{aligned} \tag{20}$$

where $\delta_j = \tilde{w}_j - \tilde{w}_0$, $f^{(m)}$ is the m-th derivative of $f(x)$, and the mappings from the values δ_j to the coefficients w_m can be precomputed and stored for different degree cases. We have developed Mathematica files for generating these precomputed tables.

To recap, numerical stability issues arise whenever a subset of roots are very close to each other. To rectify the situation, higher order derivatives become necessary in the residue theorem, and the exponential sum becomes a finite difference approximation of the derivatives. So, we have to factor the polynomial approximation in the denominator into the product of two parts: (1) a product of those clustered roots and (2) everything else as a polynomial factor. We demonstrate in the numerical section how the new representation in Eq. (20) improves the accuracy of the original QB2X representation in Eq. (2) when a subset of roots are clustered.

4. Numerical Experiments

We present preliminary numerical results to validate the analytical formulas and demonstrate the achieved accuracy for different K (for the polynomial expansion) and P (for the plane wave expansion) values and geometry setting for the double and single layer potentials. We compare the new QB2X with the classical QBX representations and address some of the resolved numerical stability issues in this section.

We first consider the straight line segment connecting $(-1,0)$ and $(1,0)$ when $s(\tilde{x}) = 0$. The double layer potential of interest is then given by

$$DLP(w) = \frac{1}{2\pi}\Im\left(\int_{-1}^{1}\frac{-\rho(\tilde{x})}{\tilde{x}-w}\mathrm{d}\tilde{x}\right). \tag{21}$$

In existing implementations which combine QBX with FMM, the density function $\rho(\tilde{x})$ is often approximated by an orthogonal polynomial expansion, e.g., the Chebyshev polynomial expansion $\rho(\tilde{x}) = \sum_{n=0}^{N} c_n T_n(\tilde{x})$ where $T_n(\tilde{x})$ is the n_{th} Chebyshev basis polynomial given by $T_n(\cos\theta) = \cos(n\theta)$. The first three basis polynomials in terms of $\tilde{x} = \cos(\theta)$ are explicitly given by $T_0(\tilde{x}) = 1$, $T_1(\tilde{x}) = \tilde{x}$, and $T_2(\tilde{x}) = 2\tilde{x}^2 - 1$. In the first numerical test, we choose 4 different density ρ functions: (a) $\rho(\tilde{x}) = \cos(\tilde{x})$; (b) $\rho(\tilde{x}) = e^{\cos(\tilde{x})}$; (c) $\rho(\tilde{x}) = T_0(\tilde{x}) + \frac{1}{2}T_1(\tilde{x}) + \frac{1}{4}T_2(\tilde{x}) = \frac{1}{4}(2\tilde{x}^2 + 2\tilde{x} + 3)$; and (d) $\rho(\tilde{x}) = \frac{1}{8}(4\tilde{x}^3 + 4\tilde{x}^2 + \tilde{x} + 6)$. For (a), as it is already in the form of an exponential expansion, so $P = 1$. We use $P = 20$ in the Fourier expansion for (b) to guarantee machine precision accuracy. For (c) and (d), we apply the precomputed mapping from the polynomial basis to the Fourier basis to compute the Fourier extensions with $P = 30$. The approximation errors are also around machine precision. We assume the target point $w \in [-\frac{1}{3}, \frac{1}{3}] \times [-\frac{2}{3}, 0]$ and the center of the leaf box is given by $w_0 = (0, \frac{-1}{3})$. For the I_1 and I_2 terms given explicitly in Eq. (10), we choose the contours in Fig. 6, where $L \to \infty$ is used. The r_{max} values are $r_{max} = 0.354$ for the upper contour and $r_{max} = 0.471$ for the lower contour, respectively. We choose $K = 40$ which guarantees at least 13-digits accuracy in the complex local Taylor polynomial expansion using standard FMM error analysis. The approximation errors are shown in the Fig. 7. For all cases, the QB2X method achieves approximately 14-digits accuracy.

In classical FMM error analysis, when $K = 9$, the complex local Taylor polynomial expansion is guaranteed to achieve 3-digits accuracy, and the accuracies increase to 6, 9, and 12 digits when $K = 18$, 27, and 36, respectively. The same error estimates can be derived using the r_{max} values in this example. In Fig. 8, we show the approximation error for different number of expansion terms K for case (c) when $\rho(\tilde{x}) = \frac{1}{4}(2\tilde{x}^2 + 2\tilde{x} + 3)$. In the experiment, we fix $P = 30$ so the error from the Fourier extension is within machine precision. For all tested K values, the errors are less than the error bound estimates derived using r_{max}.

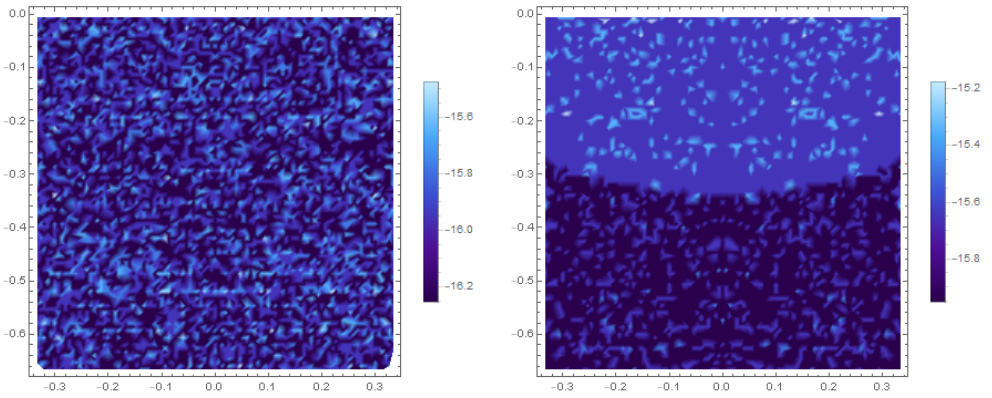

(a) $\rho(x) = \cos(x)$, $P = 1$ (b) $\rho(x) = e^{\cos(x)}$, $P = 20$

(c) $\rho(x) = \frac{1}{4}\left(2x^2 + 2x + 3\right)$, $P = 30$ (d) $\rho(x) = \frac{1}{8}\left(4x^3 + 4x^2 + x + 6\right)$, $P = 30$

Figure 7: Approximation errors of QB2X representations for double layer potentials with $K = 40$ for different density functions. The plot legends are $\log_{10}(Error)$.

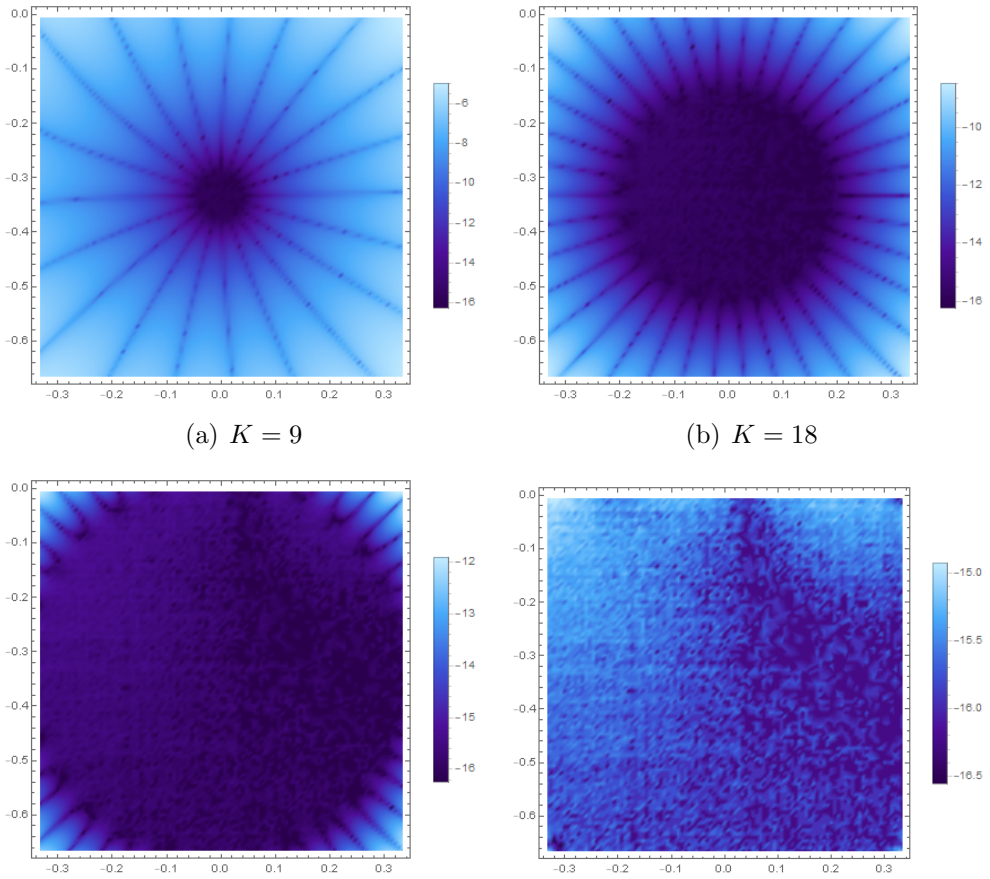

(a) $K = 9$ (b) $K = 18$

(c) $K = 27$ (d) $K = 36$

Figure 8: Approximation errors of the QB2X double layer potential representations with $\rho(\tilde{x}) = \frac{1}{4}\left(2\tilde{x}^2 + 2\tilde{x} + 3\right)$ for different K values. $P = 30$. The plot legends are $\log_{10}(Error)$.

We want to mention that the original QBX method can also produce satisfactory results for the straight line boundary setting but may require (slightly) more expansion terms for certain problems. This can be explained by studying the truncation error when a plane wave term e^{ipw} is re-expanded as a local Taylor polynomial expansion

$$e^{\mathrm{i}p(w-w_0)} = \sum_{k=0}^{\infty} \frac{(\mathrm{i}p)^k}{k!}(w-w_0)^k \tag{22}$$

where w_0 is the expansion center. We assume $|w-w_0| \leq 1$, and study how many terms are required in the polynomial expansion in order to achieve machine precision accuracy, i.e., we need to find N such that $|\sum_{k=N}^{\infty} \frac{(\mathrm{i}p)^k}{k!}(w-w_0)^k| \leq 10^{-16}$. Using the incomplete gamma function $\Gamma(N,p) = \int_p^{\infty} e^{-x}x^{N-1}\mathrm{d}x$ and gamma function $\Gamma(N) = \Gamma(N,0)$, we have

$$|\sum_{k=N}^{\infty} \frac{(\mathrm{i}p)^k}{k!}(w-w_0)^k| \leq \sum_{k=N}^{\infty} \frac{p^k}{k!} = \frac{e^p(\Gamma(N)-\Gamma(N,p))}{\Gamma(N)}.$$

In Fig. 9, we numerically solve the inequality $\frac{e^p(\Gamma(N)-\Gamma(N,p))}{\Gamma(N)} \leq 10^{-16}$ to get an estimate of N. When $p = 30$ is used in the plane wave expansion, to achieve machine precision the estimated N is about 111. Instead of presenting the detailed QBX results for the straight line case in this paper, we refer interested readers to the original QBX paper in [24].

For the curved geometry, we found that due to the extremely nonlinear relationship implicitly shown in the $s'(\tilde{w}_j)$ terms in the plane wave type expansions, more terms become necessary in the classical QBX scheme in order to achieve a prescribed accuracy requirement. In Fig. 10, we consider the double layer potential with density function $\rho(\tilde{x}) = e^{2\pi\mathrm{i}\tilde{x}} + e^{-2\pi\mathrm{i}\tilde{x}}$, $-1 < \tilde{x} < 1$, where the geometry is given by $s(\tilde{x}) = \frac{\tilde{x}^2}{2} - \frac{\tilde{x}^3}{3} - \frac{\tilde{x}^4}{3}$. As the density function is already in the form of a Fourier series, no Fourier extension computation is needed. We use this low-frequency mode in order to focus on the impacts of the boundary geometry to QBX and QB2X presentations. Accuracy and efficiency results from the QB2X methods are very similar for high frequency modes. We first plot the QBX errors for different numbers of polynomial terms K for the region $\{w = x + \mathrm{i}y : -\frac{1}{3} < x < \frac{1}{3}, -\frac{2}{3} < y < s(x)\}$. When $K = 40$, the classical QBX method only obtains results with 6 digits accuracy.

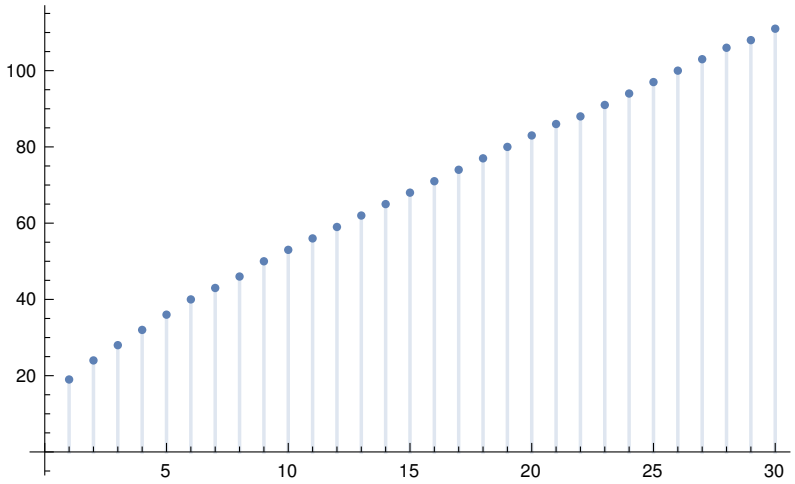

Figure 9: Estimated N (y-axis) for different wave number p (x-axis).

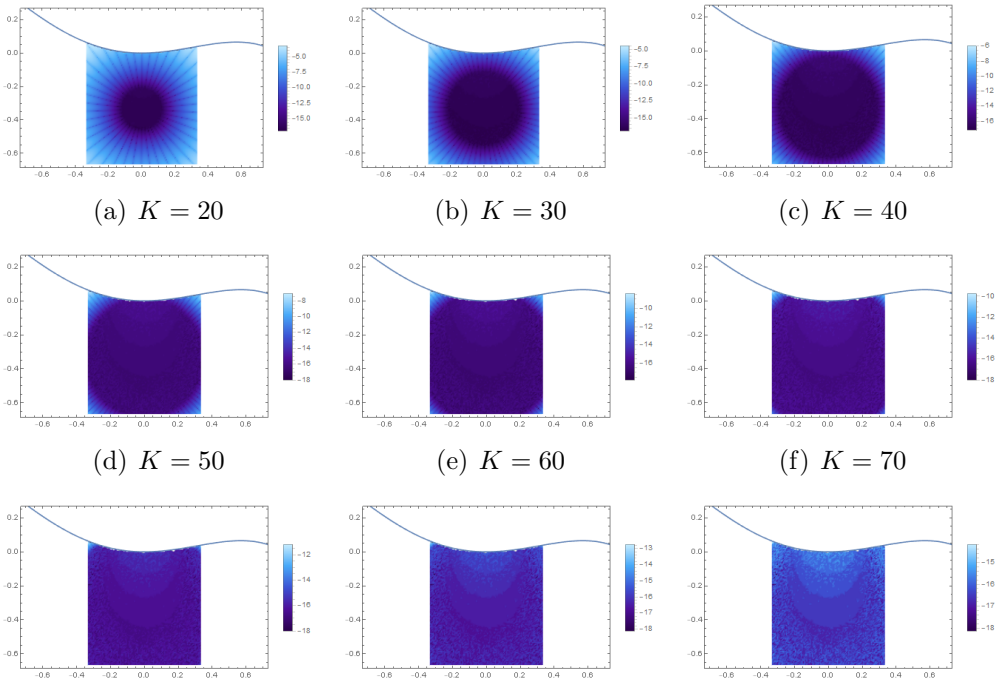

(a) $K = 20$ (b) $K = 30$ (c) $K = 40$

(d) $K = 50$ (e) $K = 60$ (f) $K = 70$

(g) $K = 80$ (h) $K = 90$ (i) $K = 100$

Figure 10: Approximation errors of the classical QBX double layer potential representation for curve $s(\tilde{x}) = \frac{\tilde{x}^2}{2} - \frac{\tilde{x}^3}{3} - \frac{\tilde{x}^4}{3}$ for different K values. The plot legends are $\log_{10}(Error)$.

In order to achieve 10^{-14} error, $K = 100$ has to be used. In many existing QBX implementations, a commonly applied strategy is to further refine the computational domain, or equivalently, introduce several QBX expansions at different centers for the same leaf box. As a comparison, in Fig. 11, we present the results using the QB2X method. The numerical results show

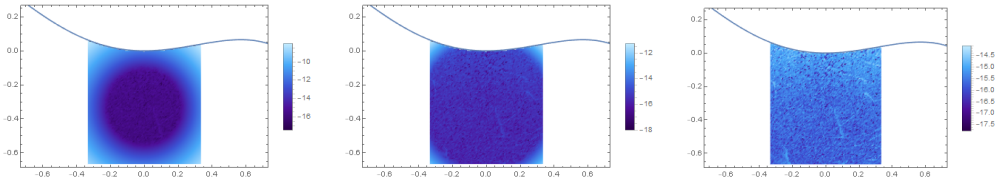

(a) $K = 20$ (b) $K = 30$ (c) $K = 40$

Figure 11: Approximation errors of the new QB2X double layer potential representations for curve $s(\tilde{x}) = \frac{\tilde{x}^2}{2} - \frac{\tilde{x}^3}{3} - \frac{\tilde{x}^4}{3}$ for different K values. The plot legends are $\log_{10}(Error)$.

that when $K = 20$, 30, and 40, the QB2X method achieves the accuracy of approximately 9.7×10^{-9}, 5.4×10^{-12}, and 8.2×10^{-15}, respectively.

We also tested both QBX and QB2X for other boundary geometry settings. We use

$$s(\tilde{x}) = -\frac{\tilde{x}^2}{3} + \tilde{x}^4$$

for the second boundary curve,

$$s(\tilde{x}) = \frac{\tilde{x}^2}{3} + \frac{\tilde{x}^3}{10} - \frac{\tilde{x}^4}{2}$$

for curve 3, and

$$s(\tilde{x}) = \tilde{x}^2 + \frac{\tilde{x}^3}{10} - 2\tilde{x}^4$$

for curve 4. In Fig. 12, we present the errors from the original QBX method for different K values. It is clear that in order to achieve a prescribed accuracy requirement in the region $\{w = x + \mathrm{i}y : -\frac{1}{3} < x < \frac{1}{3}, -\frac{2}{3} < y < s(x)\}$, more terms (than from classical FMM analysis) are required if one single polynomial expansion is used. In particular, for curve 4, even though the errors decay rapidly in the regions close to the expansion center, because of the extreme nonlinear dependency on the geometry, the $||err||_\infty$ values are 6.0×10^{-2}, 2.5×10^{-2}, and 1.9×10^{-2} when $K = 40$, $K = 60$, and $K = 100$, respectively. This very slow convergence means that several expansions

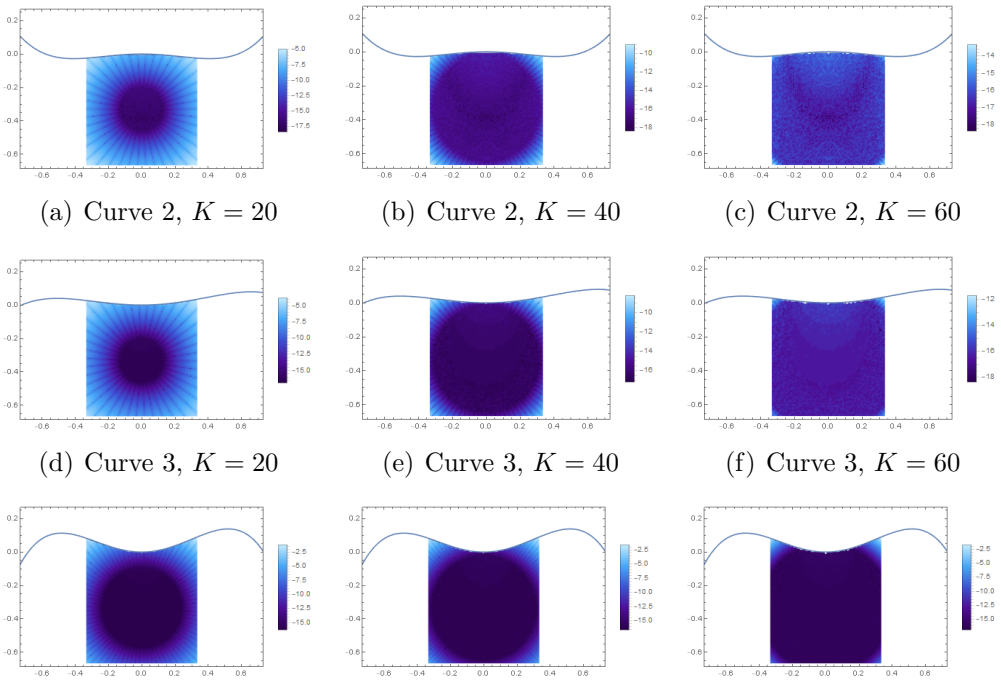

(a) Curve 2, $K = 20$ (b) Curve 2, $K = 40$ (c) Curve 2, $K = 60$

(d) Curve 3, $K = 20$ (e) Curve 3, $K = 40$ (f) Curve 3, $K = 60$

(g) Curve 4, $K = 40$ (h) Curve 4, $K = 60$ (i) Curve 4, $K = 100$

Figure 12: Approximation errors of the classical QBX double layer potential representations for curves 2, 3, and 4 for different K values. The plot legends are $\log_{10}(Error)$.

with different expansion centers have to be used for the interested region $\{w = x + \mathrm{i}y : -\frac{1}{3} < x < \frac{1}{3}, -\frac{2}{3} < y < s(x)\}$. In many existing QBX+FMM implementations, this is achieved by either requesting more refinement levels in the FMM hierarchical adaptive tree structures, or using several expansions with different centers in the same leaf box, or both. As a comparison, in Fig. 13, we present the results for the QB2X method for different K values. For all the curves, the errors from the new QB2X method are bounded by the theoretical results from standard FMM analysis.

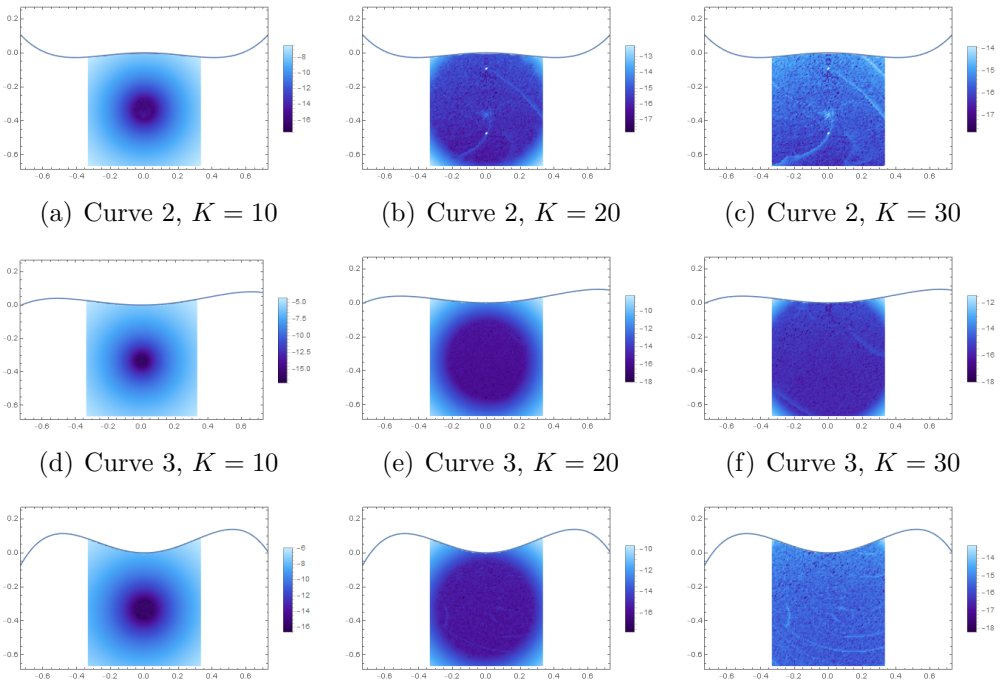

(a) Curve 2, $K = 10$ (b) Curve 2, $K = 20$ (c) Curve 2, $K = 30$

(d) Curve 3, $K = 10$ (e) Curve 3, $K = 20$ (f) Curve 3, $K = 30$

(g) Curve 4, $K = 10$ (h) Curve 4, $K = 20$ (i) Curve 4, $K = 30$

Figure 13: Approximation errors of the new QB2X double layer potential representations for curves 2, 3, and 4 for different K values. The plot legends are $\log_{10}(Error)$.

When some of the roots of the polynomial equation $z + \mathrm{i}s(z) - w = 0$ are close to each other, the standard exponential sum suffers from the same type of numerical instability as in difference approximation of the derivatives, and one has to apply Eq. (20) to accurately compute the potential. We demonstrate this phenomenon using the geometry setting

$$s(\tilde{x}) = -\frac{\tilde{x}^2}{5} - \frac{\tilde{x}^3}{3} - \frac{\tilde{x}^4}{3}.$$

For the evaluation point $w = \frac{47}{150} - \frac{1}{3}\mathrm{i}$, the polynomial equation $z + \mathrm{i}s(z) - w = 0$ has the roots

$$\begin{aligned}
\tilde{w}_1 &= -1.615679579247955 - 0.692156051488856\mathrm{i}, \\
\tilde{w}_2 &= 0.525640932633123 - 0.464669127597158\mathrm{i}, \\
\tilde{w}_3 &= -0.403752027667708 + 1.610266304338427\mathrm{i}, \text{ and} \\
\tilde{w}_4 &= 0.493790674282540 - 0.453441125252414\mathrm{i}.
\end{aligned}$$

Note that both $\tilde{w}_2$ and $\tilde{w}_4$ are located in the lower half complex plane and are close to each other, $\tilde{w}_2 - \tilde{w}_4 \approx 0.032 + 0.011\mathrm{i}$, therefore direct application of Eq. (18) to compute I_2 will lose about 2 digits accuracy. Using the density function $\rho(\tilde{x}) = e^{-2\pi \mathrm{i}\tilde{x}}$, we compared the numerically computed I_2 value using Eq. (18) with a reference solution with 20 correct digits derived using Mathematica, and found the numerical error is $4.52 \times 10^{-13} + 1.86 \times 10^{-13}\mathrm{i}$, which is approximately of the magnitude $|\frac{\text{machine precision}}{\tilde{w}_2 - \tilde{w}_4}|$. However, when Eq. (20) is applied, the error becomes $6.21 \times 10^{-15} + 2.44 \times 10^{-15}\mathrm{i}$ which is about machine precision.

We also present the QB2X results for the single layer potentials. We firstly consider the straight line case for different density functions defined on the line segment connecting $(-1, 0)$ and $(1, 0)$. We use the same density functions as those in the double layer case, and the approximation errors are shown in Fig. 14 when $K = 40$. For all cases, we achieve 14-digits accuracy. To demonstrate the error dependency on the number of local Taylor polynomial expansion terms K, in Fig. 15, we plot the errors for different K values when $\rho(\tilde{x}) = \frac{1}{4}(2\tilde{x}^2 + 2\tilde{x} + 3)$. Similar to the double layer case, for all tested K values, the errors are smaller than the estimated bounds.

Finally we consider the single layer potential on a curved boundary

$$s(\tilde{x}) = -\frac{1}{10}\tilde{x}^2$$

when $\rho(\tilde{x}) = \frac{1}{4}(2\tilde{x}^2 + 2\tilde{x} + 3)$ for different K values. The single layer potential is given by

$$SLP(w) = \frac{1}{4\pi} \int_{-1}^{1} \log((x - \tilde{x})^2 + (y + \frac{1}{10}\tilde{x}^2)^2)\tilde{\rho}(\tilde{x})\mathrm{d}\tilde{x} \tag{23}$$

where $\tilde{\rho}(\tilde{x}) = \rho(\tilde{x})\sqrt{1 + \frac{\tilde{x}^2}{25}}$. In the left plot of Fig. 16, we show the error distribution when $K = 18$ terms are used in the polynomial expansion. The

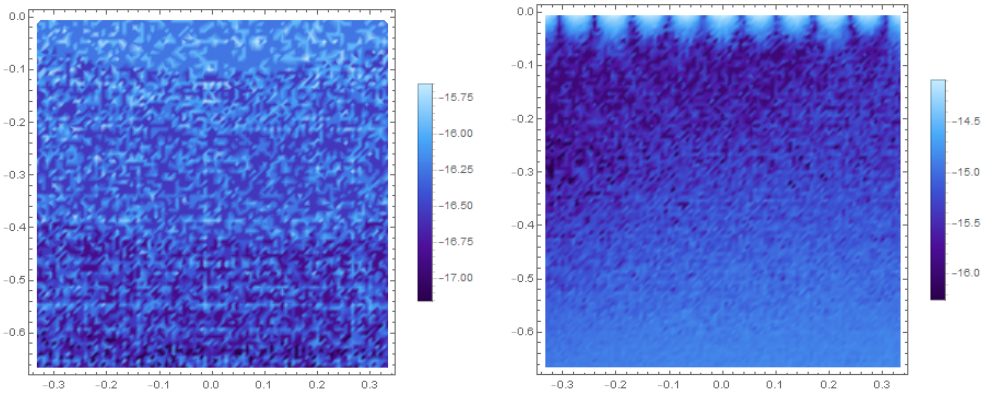

(a) $\rho(\tilde{x}) = \cos(\tilde{x})$, $P = 1$

(b) $\rho(\tilde{x}) = e^{\cos(\tilde{x})}$, $P = 20$

(c) $\rho(\tilde{x}) = \frac{1}{4}\left(2\tilde{x}^2 + 2\tilde{x} + 3\right)$, $P = 30$

(d) $\rho(\tilde{x}) = \frac{1}{8}\left(4\tilde{x}^3 + 4\tilde{x}^2 + \tilde{x} + 6\right)$, $P = 30$

Figure 14: QB2X approximation errors of single layer potential for $K = 40$ and different density functions. The boundary is a line segment connecting $(-1, 0)$ and $(1, 0)$. The plot legends are $\log_{10}(Error)$.

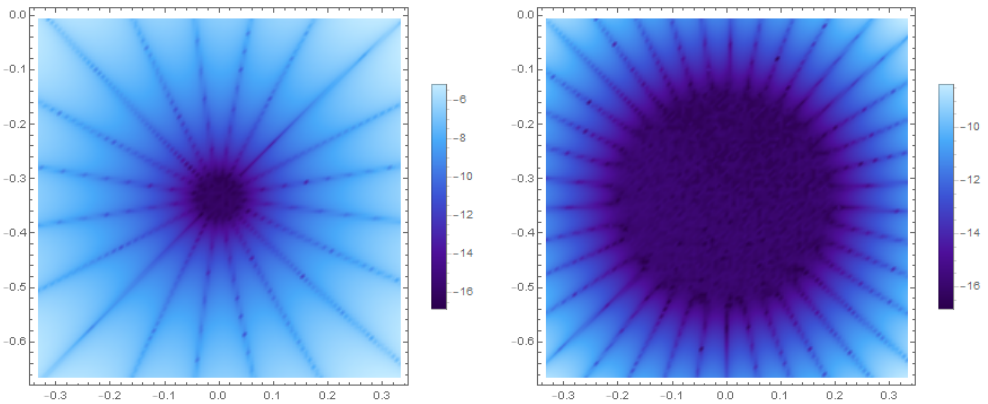

(a) $K = 9$

(b) $K = 18$

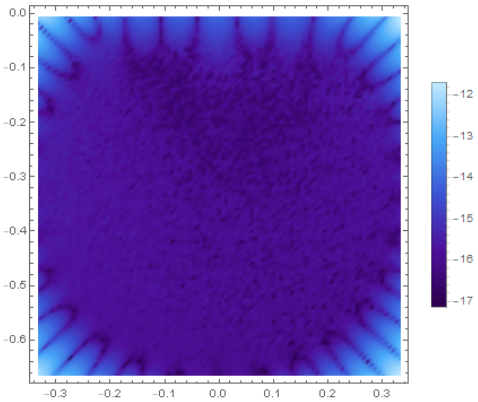

(c) $K = 27$

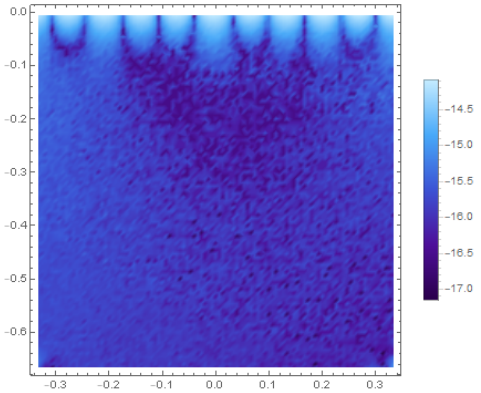

(d) $K = 36$

Figure 15: QB2X approximation errors of single layer potential for $P = 30$ and density function $\rho(\tilde{x}) = \frac{1}{4}\left(2\tilde{x}^2 + 2\tilde{x} + 3\right)$. The boundary is a line segment connecting $(-1, 0)$ and $(1, 0)$. The plot legends are $\log_{10}(Error)$.

computed numerical results achieve at least 6-digits accuracy. In the right plot, we show the error when $K = 36$, and the results have approximately 14-digits accuracy.

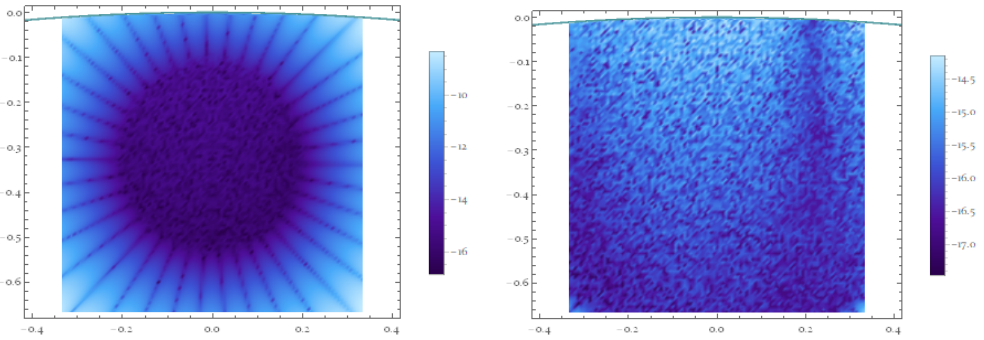

(a) $K = 18$ (b) $K = 36$

Figure 16: QB2X approximation errors of single layer potential for different K, $P = 30$ and density functions $\rho(\tilde{x}) = \frac{1}{4}\left(2\tilde{x}^2 + 2\tilde{x} + 3\right)$. The boundary is $(\tilde{x}, -\frac{1}{10}\tilde{x}^2)$. The plot legend is $\log_{10}(Error)$.

5. Summary

In this paper, we present a new quadrature by two expansions (QB2X) method for the Laplace layer potentials in two dimensions. Both the local complex Taylor polynomial expansion and plane wave type expansions are used in the new representation. Compared with the classical QBX, the new QB2X representations allow easier error analysis. For a prescribed accuracy requirement, the QB2X representations are valid in a much larger region when compared with classical QBX representations. The impact of the boundary geometry also becomes explicit in the QB2X representations, providing a useful tool for PDE analysis.

The QB2X technique can be generalized to other types of equations (e.g., the Helmholtz and Yukawa equations) in both two and three dimensions using the Green's Identities. In these cases, the local complex Taylor polynomial expansions become the well-know partial wave expansions. The partial wave and plane wave basis functions form a frame, and the combined QB2X representations should have improved accuracy, stability and efficiency properties and can be easily combined with existing fast multipole methods when solv-

ing boundary value elliptic PDE problems. Results along these directions will be presented in subsequent papers.

Acknowledgement

We thankfully acknowledge the generous support of the NSF grants DMS-1821093 (Huang) and NSF CAREER Grant DMS-1352353 and grant DMS-1909035 (Marzuola). Part of the results was based on the work during the *Fast and Accurate Simulation of Waves in Layered Media* Collaborate@ICERM workshop while some of the authors were in residence at the Institute for Computational and Experimental Research in Mathematics (ICERM) in Providence, RI supported by the National Science Foundation under Grant No. DMS-1439786.

References

[1] J. C. Aguilar and Y. Chen. High-order corrected trapezoidal quadrature rules for functions with a logarithmic singularity in 2-d. *Computers & Mathematics with Applications*, 44(8-9):1031–1039, 2002.

[2] B. K. Alpert. Hybrid gauss-trapezoidal quadrature rules. *SIAM Journal on Scientific Computing*, 20(5):1551–1584, 1999.

[3] A. Barnett, B. Wu, and S. Veerapaneni. Spectrally accurate quadratures for evaluation of layer potentials close to the boundary for the 2d stokes and laplace equations. *SIAM Journal on Scientific Computing*, 37(4):B519–B542, 2015.

[4] J. T. Beale and M.-C. Lai. A method for computing nearly singular integrals. *SIAM Journal on Numerical Analysis*, 38(6):1902–1925, 2001.

[5] J. P. Boyd. A comparison of numerical algorithms for fourier extension of the first, second, and third kinds. *Journal of Computational Physics*, 178(1):118–160, 2002.

[6] J. Bremer, Z. Gimbutas, and V. Rokhlin. A nonlinear optimization procedure for generalized gaussian quadratures. *SIAM Journal on Scientific Computing*, 32(4):1761–1788, 2010.

[7] J. Bremer, V. Rokhlin, and I. Sammis. Universal quadratures for boundary integral equations on two-dimensional domains with corners. *Journal of Computational Physics*, 229(22):8259–8280, 2010.

[8] O. P. Bruno, Y. Han, and M. M. Pohlman. Accurate, high-order representation of complex three-dimensional surfaces via fourier continuation analysis. *Journal of computational Physics*, 227(2):1094–1125, 2007.

[9] O. P. Bruno and L. A. Kunyansky. A fast, high-order algorithm for the solution of surface scattering problems: basic implementation, tests, and applications. *Journal of Computational Physics*, 169(1):80–110, 2001.

[10] P. G. Casazza and G. Kutyniok. *Finite frames: Theory and applications*. Springer, 2012.

[11] H. Cheng, W. Y. Crutchfield, Z. Gimbutas, L. F. Greengard, J. F. Ethridge, J. Huang, V. Rokhlin, N. Yarvin, and J. Zhao. A wideband fast multipole method for the helmholtz equation in three dimensions. *Journal of Computational Physics*, 216(1):300–325, 2006.

[12] W. Crutchfield, Z. Gimbutas, L. Greengard, J. Huang, V. Rokhlin, N. Yarvin, and J. Zhao. Remarks on the implementation of wideband fmm for the helmholtz equation in two dimensions. *Contemporary Mathematics*, 408:99–110, 2006.

[13] F. De Terán, F. M. Dopico, and J. Pérez. Backward stability of polynomial root-finding using fiedler companion matrices. *IMA Journal of Numerical Analysis*, 36(1):133–173, 2016.

[14] R. J. Duffin and A. C. Schaeffer. A class of nonharmonic fourier series. *Transactions of the American Mathematical Society*, 72(2):341–366, 1952.

[15] M. G. Duffy. Quadrature over a pyramid or cube of integrands with a singularity at a vertex. *SIAM journal on Numerical Analysis*, 19(6):1260–1262, 1982.

[16] C. L. Epstein, L. Greengard, and A. Klockner. On the convergence of local expansions of layer potentials. *SIAM Journal on Numerical Analysis*, 51(5):2660–2679, 2013.

[17] L. Greengard. *The rapid evaluation of potential fields in particle systems*. MIT press, 1988.

[18] L. Greengard and V. Rokhlin. A fast algorithm for particle simulations. *Journal of computational physics*, 73(2):325–348, 1987.

[19] L. Greengard and V. Rokhlin. A new version of the fast multipole method for the laplace equation in three dimensions. *Acta numerica*, 6:229–269, 1997.

[20] W. Hackbusch and S. A. Sauter. On numerical cubatures of nearly singular surface integrals arising in bem collocation. *Computing*, 52(2):139–159, 1994.

[21] J. Helsing and R. Ojala. On the evaluation of layer potentials close to their sources. *Journal of Computational Physics*, 227(5):2899–2921, 2008.

[22] D. Huybrechs. On the fourier extension of nonperiodic functions. *SIAM Journal on Numerical Analysis*, 47(6):4326–4355, 2010.

[23] S. Kapur and V. Rokhlin. High-order corrected trapezoidal quadrature rules for singular functions. *SIAM Journal on Numerical Analysis*, 34(4):1331–1356, 1997.

[24] A. Klöckner, A. Barnett, L. Greengard, and M. O'Neil. Quadrature by expansion: A new method for the evaluation of layer potentials. *Journal of Computational Physics*, 252:332–349, 2013.

[25] D. W. Lozier. Nist digital library of mathematical functions. *Annals of Mathematics and Artificial Intelligence*, 38(1-3):105–119, 2003.

[26] J. Ma, V. Rokhlin, and S. Wandzura. Generalized gaussian quadrature rules for systems of arbitrary functions. *SIAM Journal on Numerical Analysis*, 33(3):971–996, 1996.

[27] O. Marin, O. Runborg, and A.-K. Tornberg. Corrected trapezoidal rules for a class of singular functions. *IMA Journal of Numerical Analysis*, 34(4):1509–1540, 2014.

[28] K. Nabors and J. White. Fastcap: A multipole accelerated 3-d capacitance extraction program. *IEEE Transactions on Computer-Aided Design of Integrated Circuits and Systems*, 10(11):1447–1459, 1991.

[29] F. Olver, D. Lozier, R. Boisvert, and C. Clark. Digital library of mathematical functions: Online companion to nist handbook of mathematical functions (cup). *National Insitute of Standards and Technology, Gaithersburg*, 2010.

[30] M. Rachh, A. Klöckner, and M. O'Neil. Fast algorithms for quadrature by expansion i: Globally valid expansions. *Journal of Computational Physics*, 345:706–731, 2017.

[31] J. Strain. Locally corrected multidimensional quadrature rules for singular functions. *SIAM Journal on Scientific Computing*, 16(4):992–1017, 1995.

[32] N. Yarvin and V. Rokhlin. Generalized gaussian quadratures and singular value decompositions of integral operators. *SIAM Journal on Scientific Computing*, 20(2):699–718, 1998.